

University of Groningen

## Discrete Dislocation Plasticity Analysis of Cracks and Fracture

Giessen, Erik van der

*Published in:*

MULTISCALE MODELLING OF PLASTICITY AND FRACTURE BY MEANS OF DISLOCATION MECHANICS

**IMPORTANT NOTE:** You are advised to consult the publisher's version (publisher's PDF) if you wish to cite from it. Please check the document version below.

*Document Version*

Publisher's PDF, also known as Version of record

*Publication date:*

2010

[Link to publication in University of Groningen/UMCG research database](#)

*Citation for published version (APA):*

Giessen, E. V. D. (2010). Discrete Dislocation Plasticity Analysis of Cracks and Fracture. In R. Pippan, & P. Gumbsch (Eds.), *MULTISCALE MODELLING OF PLASTICITY AND FRACTURE BY MEANS OF DISLOCATION MECHANICS* (522 ed., pp. 185-212). (CISM Courses and Lectures; Vol. 522). Springer.

### Copyright

Other than for strictly personal use, it is not permitted to download or to forward/distribute the text or part of it without the consent of the author(s) and/or copyright holder(s), unless the work is under an open content license (like Creative Commons).

The publication may also be distributed here under the terms of Article 25fa of the Dutch Copyright Act, indicated by the "Taverne" license. More information can be found on the University of Groningen website: <https://www.rug.nl/library/open-access/self-archiving-pure/taverne-amendment>.

### Take-down policy

If you believe that this document breaches copyright please contact us providing details, and we will remove access to the work immediately and investigate your claim.

*Downloaded from the University of Groningen/UMCG research database (Pure): <http://www.rug.nl/research/portal>. For technical reasons the number of authors shown on this cover page is limited to 10 maximum.*

# Discrete Dislocation Plasticity Analysis of Cracks and Fracture

Erik Van der Giessen

Dept. of Applied Physics, University of Groningen, Nijenborgh 4, 9747 AG Groningen,  
The Netherlands

## 1 Introduction

Fracture in plastically deforming crystals involves several length scales, as illustrated in Fig. 1 for cleavage-like crack growth. The relevant length scales range from that of the macroscale object to the atomic scale, including the various microstructural length scales in between that are associated with, for example, particles, grains, and defect structures.

At the large length scale of the macroscopic world, Fig. 1a, plastic deformation is conveniently described by a phenomenological continuum theory. The stress field near the tip of a mathematically sharp crack tip then is singular at the tip, Fig. 1b. At the scale where the polycrystalline nature is revealed, Fig. 1c, plastic deformation is a physical process that is inherently inhomogeneous and anisotropic. This is caused by the fact that each grain is anisotropic with a finite number of slip systems on which glide can take place. When zooming in further, one will see that plastic deformation within each grain involves the collective motion of many dislocations, Fig. 1d. Finally, the finest scale shown in Fig. 1e governs where atomic bonds are broken upon crack propagation.

The challenge in understanding fracture lies in the fact that all scales are connected and all may contribute to the total fracture energy. It is worth emphasizing that although the atomistics of the separation of surfaces may only contribute a small fraction of the total energy release rate, it can still be controlling. This is because dissipative mechanisms can only operate if fracture is delayed sufficiently to allow them to come into play. Indeed, as pointed out by Rice and Wang [28], the surface energy can play a valve-like role. Surface energies are typically of the order of  $1 \text{ J/m}^2$ , while fracture energies for ductile crystalline metals are often an order of magnitude higher. The difference between the fracture energy and the surface energy is the plastic dissipation in the vicinity of the crack tip. Many details are left out in the above discussion, but it emphasizes that fracture, i.e. the creation of new surface, is highly localized at the atomic scale, but is driven by

the macroscopic applied load communicated to the atomic scale via stress fields on smaller and smaller length scales. It is the precise communication down these scales which determines whether or not crack growth occurs and how much energy is dissipated.

Much is known about the near crack-tip fields at the continuum scale. At the polycrystalline scale, and if the average response is isotropic, the smooth HRR plastic fields developed by Hutchinson [18] and by Rice and Rosengren [26] are dominant, while the fields change to a completely different nature, characterized by piece-wise uniform sectors [27, 29, 30], when the crack tip is contained in a single crystal. At the latter scale of observation, i.e. in between Fig. 1c and d, the theories predict near-tip stresses that are a few times the yield strength. This is far below the atomic bond strength, thus raising the ‘paradox’ that crack growth

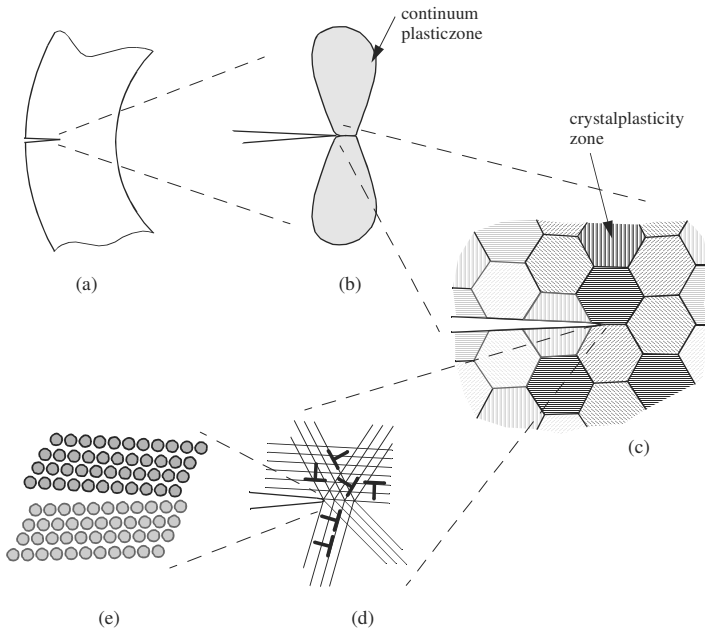


**Figure 1.** The various relevant scales that may determine the response of a crack in a macroscopic component. (a) The component scale. (b) The plastic zone governed by macroscopic continuum plastic flow. (c) The grain scale in a polycrystalline metal. (d) The scale of discrete slip planes and of individual dislocations. (e) The atomic scale.

could not occur in plastically deforming materials. Experience proves us wrong. This chapter intends to present insight in resolving this, principally by describing plastic deformation by the generation and motion of discrete dislocations, i.e. the size scale of Fig. 1d. An introduction to *discrete dislocation plasticity* may be found in [5]; a short summary is included in the first two sections.

## 2 Elastic Models of Dislocations

### 2.1 General Idea

A dislocation is a line defect in an atomic lattice ([17, 16]). It is a line on an atomic plane that separates those regions of the plane that are intact from regions where the lattice has undergone slip. The relative shift of atomic planes is in the direction denoted by the Burgers vector  $\mathbf{b}$  and is essentially uniform in the region enclosed by the dislocation. The dislocated material can be constructed in a thought experiment from a perfect crystal by a cut-displace by  $\mathbf{b}$ -and-reweld procedure. Because of conservation of mass, a dislocation is a closed loop.

The geometry of a dislocation is governed by a number of variables:

- the slip plane, denoted with its unit normal vector  $\mathbf{m}$ ;
- the dislocation line as a parameterized line on this plane and with a local tangent vector  $\mathbf{t}$ ;
- the Burgers vector  $\mathbf{b}$ .

There are a few special parts of a generic loop, namely

$$\text{edge: } \mathbf{b} \cdot \mathbf{t} = 0; \quad (1)$$

$$\text{screw: } \mathbf{b} \cdot \mathbf{t} = \pm b, \quad (2)$$

$b$  being the length of  $\mathbf{b}$ :  $b = |\mathbf{b}|$ . Edge and screw dislocations are the central notions in two-dimensional studies, see Fig. 2. As the crack problems studied later on in this chapter are concerned with mode I, plane strain conditions, attention will be focused on edge dislocations.

Although a dislocation is a lattice defect, it has proved very useful to describe it in the framework of continuum theory in which the atomic positions are averaged out. This reduces the total number of degrees of freedom enormously: from all atom positions to a mathematical, functional form of the geometric variables  $\mathbf{m}$ ,  $\mathbf{t}$  and  $\mathbf{b}$ . In a continuum framework the definition of the Burgers vector becomes

$$\mathbf{b} = \oint_C \frac{\partial \mathbf{u}}{\partial c} dc \quad (3)$$

where  $C$  is a closed circuit around the dislocation, traversed by local coordinate  $c$  and  $\mathbf{u}$  is the displacement field away from the perfect crystal. The real key to

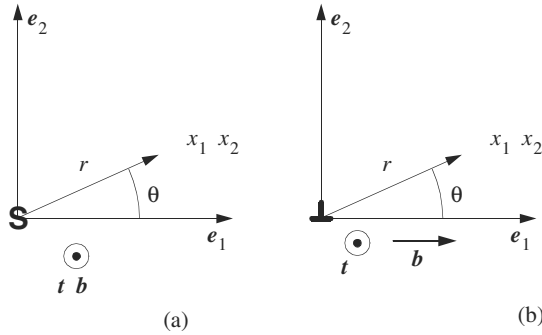


**Figure 2.** Definitions of (a) screw and (b) edge dislocation configurations discussed in the text.

dislocations in a continuum description is that it involves a *displacement discontinuity* inside the dislocation loop. It is the expansion of dislocation loops that creates what we observe on a larger scale as *permanent*, that is, *plastic deformation*. Apart from the dislocation motion, the distortion of the lattice is entirely elastic. Thus, the picture of plasticity emerges of dislocation loops sweeping through an otherwise elastic continuum.

The current continuum theory of discrete dislocations employs linear elasticity. Clearly, it will break down inside the core region, where the strains will be too large for the linear approximation to hold. Away from the core by about 5 to  $6b$ , comparison with atomistics has shown that the linear elastic solution is very accurate. Hence, discrete dislocation plasticity holds the view that the fields in a dislocated body can be described by linear elasticity, excluding the core regions. The use of linear elasticity has the enormous advantage that many solutions for the governing equations are known and that one can use superposition. The latter will be exploited in full power in Sec. 3.

For completeness, we recall that the governing equations for linear elasticity are

$$\text{equilibrium} : \sigma_{ij,j} = 0 \quad (4)$$

$$\text{elasticity} : \sigma_{ij} = \mathcal{L}_{ijkl} \epsilon_{kl} \quad (5)$$

$$\text{strains} : \epsilon_{ij} = \frac{1}{2}(u_{i,j} + u_{j,i}) \quad (6)$$

with  $\mathcal{L}_{ijkl}$  the elastic moduli. Since the crystals we shall consider here are cubic, we should be using the cubic elastic moduli expressed in terms of the usual  $C_{11}$ ,  $C_{12}$  and  $C_{44}$ . However, for simplicity, we will assume isotropic elasticity, with the

moduli expressed either in terms of Young's modulus  $E$  and Poisson's ratio  $\nu$ ,

$$\mathcal{L}_{ijkl} = \frac{E}{1+\nu} \left[ \frac{1}{2} (\delta_{ik}\delta_{jl} + \delta_{il}\delta_{jk}) + \frac{\nu}{1-2\nu} \delta_{ij}\delta_{kl} \right] \quad (7)$$

or as

$$\mathcal{L}_{ijkl} = \mu (\delta_{ik}\delta_{jl} + \delta_{il}\delta_{jk}) + (k - \frac{2}{3}\mu) \delta_{ij}\delta_{kl}. \quad (8)$$

in terms of the shear modulus  $\mu = E/2(1+\nu)$  and the bulk (or compression) modulus  $k = E/3(1-2\nu)$ .

## 2.2 Edge Dislocations

An *edge dislocation* poses a plane strain problem. If the dislocation line is arranged with its line direction perpendicular to the  $x_1$ - $x_2$  plane of consideration, i.e.  $\mathbf{t} = \mathbf{e}_3$ , the Burgers vector lies in the  $x_1$ - $x_2$  plane, Fig. 2b. Specifically, we shall assume again that the  $x_1$ - $x_3$  plane is the slip plane and that  $\mathbf{b}$  points in the positive  $x_1$  direction, see Fig. 2b. This problem is then conveniently solved by application of the Airy stress function approach in a manner that is similar to that leading to the asymptotic singular field near a sharp crack tip. Leaving the details to [16], the solution reads

$$\sigma_{11} = -\frac{\mu b}{2\pi(1-\nu)} \frac{x_2(3x_1^2 + x_2^2)}{(x_1^2 + x_2^2)^2} \quad (9)$$

$$\sigma_{22} = \frac{\mu b}{2\pi(1-\nu)} \frac{x_2(x_1^2 - x_2^2)}{(x_1^2 + x_2^2)^2} \quad (10)$$

$$\sigma_{12} = \frac{\mu b}{2\pi(1-\nu)} \frac{x_1(x_1^2 - x_2^2)}{(x_1^2 + x_2^2)^2} \quad (11)$$

for the in-plane stress components, while  $\sigma_{33} = \nu(\sigma_{11} + \sigma_{22})$ . As for a screw dislocation, the stress field is singular at the dislocation and decays with the distance  $r$  as  $1/r$ . The displacement field is given by

$$u_1 = \frac{b}{2\pi(1-\nu)} \left[ \frac{1}{2} \frac{x_1 x_2}{x_1^2 + x_2^2} - (1-\nu) \arctan\left(\frac{x_1}{x_2}\right) \right] \quad (12)$$

$$u_2 = \frac{b}{2\pi(1-\nu)} \left[ \frac{1}{2} \frac{x_2^2}{x_1^2 + x_2^2} - \frac{1}{4} (1-2\nu) \ln \frac{x_1^2 + x_2^2}{b^2} \right] \quad (13)$$

The  $u_1$  field, i.e. parallel to the slip plane, is shown in Fig. 3.

Note that the solution for the edge dislocation field assumes the body to be infinitely large – no boundary conditions have been incorporated. Since the solution is singular, as the solution for a screw dislocation, it is to be expected that a correction due to boundary conditions has no significant effect close to the dislocation, but it will do so at larger distances.

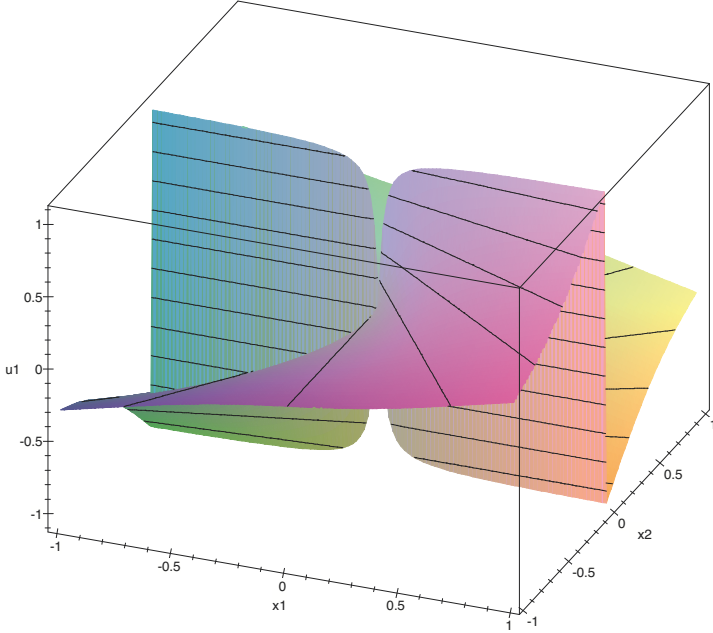


**Figure 3.** Displacement field  $u_1(x_1, x_2)$ , normalized by  $b/2\pi(1-\nu)$ , of an edge dislocation with  $\mathbf{b} = b\mathbf{e}_1$  at  $(x_1, x_2) = (0, 0)$ .

### 3 Boundary Value Problems

Even for straight two-dimensional dislocations, as discussed in the previous section, known closed-form solutions do not incorporate any boundaries of the crystal. The solutions are, strictly speaking, for dislocations in infinite space. Interactions with the boundaries of course do exist, and their are commonly [16] referred to as *image effects*. Rather clever image constructions have been developed but they remain limited to particular configurations.

Several years ago, Van der Giessen and Needleman [33] proposed a versatile approach based on superposition. The idea is to make use of the known solutions in infinite space and to superpose an ‘image’ solution to correct for the boundary conditions. To this end, the displacement, strain and stress fields are decomposed as

$$\mathbf{u} = \tilde{\mathbf{u}} + \hat{\mathbf{u}}, \quad \boldsymbol{\varepsilon} = \tilde{\boldsymbol{\varepsilon}} + \hat{\boldsymbol{\varepsilon}}, \quad \boldsymbol{\sigma} = \tilde{\boldsymbol{\sigma}} + \hat{\boldsymbol{\sigma}}. \quad (14)$$

The  $(\tilde{\phantom{x}})$  fields are the superposition of the singular fields of the individual disloca-

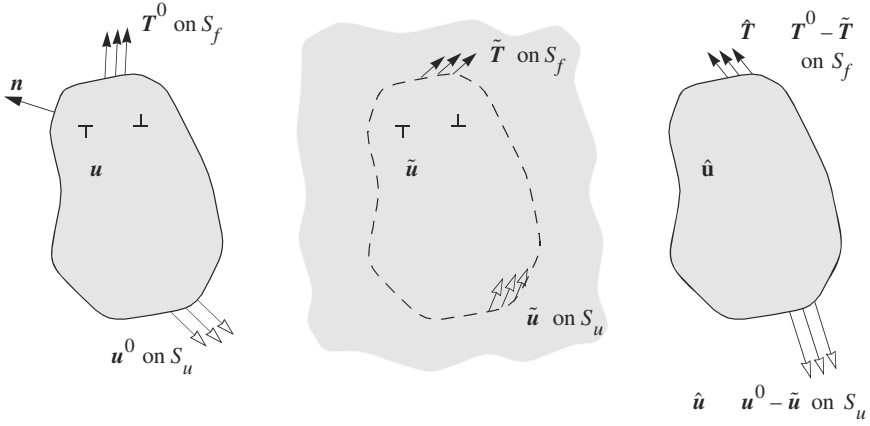


**Figure 4.** Decomposition of the problem for the dislocated body into the problem of interacting dislocations in an infinite solid ( $\tilde{\phantom{x}}$  fields) and the complementary problem for the body without dislocations ( $\hat{\phantom{x}}$  fields).

tions, as discussed above, in infinite space. Identifying the fields for dislocation  $I$  by a superscript ( $I$ ), the ( $\tilde{\phantom{x}}$ ) stress field, for example, is obtained as

$$\tilde{\boldsymbol{\sigma}} = \sum_I \boldsymbol{\sigma}^{(I)}$$

The ( $\tilde{\phantom{x}}$ ) fields will in general not meet the boundary conditions in terms of tractions on part  $S_f$  of the boundary nor the prescribed displacements on part  $S_u$ . Instead they will give rise to displacements  $\tilde{\mathbf{u}}$  on  $S_u$  and tractions  $\tilde{\mathbf{T}} = \tilde{\boldsymbol{\sigma}} \cdot \mathbf{n}$  on  $S_f$  (with normal  $\mathbf{n}$ ). The actual boundary conditions,  $\mathbf{u}^0$  on  $S_u$  and  $\mathbf{T}^0$  on  $S_f$ , are imposed through the ( $\hat{\phantom{x}}$ ) fields, in such a way that the sum of the ( $\tilde{\phantom{x}}$ ) and the ( $\hat{\phantom{x}}$ ) fields in (14) gives the solution that satisfies all boundary conditions. Since the ( $\tilde{\phantom{x}}$ ) fields satisfy the governing equations (4)–(6), the ( $\hat{\phantom{x}}$ ) fields also have to satisfy the elasticity equations, i.e.

$$\text{equilibrium: } \operatorname{div} \hat{\boldsymbol{\sigma}} = 0$$

$$\text{elasticity: } \hat{\boldsymbol{\sigma}} = \mathbf{L} : \hat{\boldsymbol{\varepsilon}}$$

$$\text{strains: } \hat{\boldsymbol{\varepsilon}} = \frac{1}{2} [\operatorname{grad} \hat{\mathbf{u}} + (\operatorname{grad} \hat{\mathbf{u}})^T]$$

supplemented with the boundary conditions

$$\hat{\mathbf{T}} = \mathbf{T}^0 - \tilde{\mathbf{T}} \text{ on } S_f \quad \hat{\mathbf{u}} = \mathbf{u}^0 - \tilde{\mathbf{u}} \text{ on } S_u$$



It is important to note that the solution of the  $(\hat{\cdot})$  problem does not involve any dislocations. Therefore, the  $(\hat{\cdot})$  fields (often called ‘image’ fields) are smooth and the boundary value problem for them can conveniently be solved using a finite element method.

A crucial concept for the evolution of dislocations, to be discussed in the next section, is the *Peach–Koehler* force. It is defined as the configurational force associated to motion of the dislocations: the work of these forces as the dislocations move is the change in *potential energy*  $\Pi$ , i.e.

$$\delta\Pi = - \sum_I \oint_{L^{(I)}} \mathbf{f}^{(I)} \cdot \delta \mathbf{s}^{(I)} dl.$$

It is seen that  $\mathbf{f}^{(I)}$  has the dimension of force per unit (dislocation line) length and that it generally changes along the loop. The Peach–Koehler force can be made more explicit, in this superposition approach, by calculating the potential energy [33]. The final result is that the component of the Peach–Koehler force in the glide plane and in the direction  $\mathbf{t}^{(I)} \times \mathbf{m}^{(I)}$  normal to the dislocation can be expressed as

$$\mathbf{f}^{(I)} = \mathbf{m}^{(I)} \cdot \left( \hat{\boldsymbol{\sigma}} + \sum_{J \neq I} \boldsymbol{\sigma}^{(J)} \right) \cdot \mathbf{b}^{(I)}. \quad (15)$$

## 4 Dislocation Dynamics

So far, we have discussed the state of the material in the presence of dislocations, but they have to move in order to produce plastic deformation. In this section, we give a brief summary of various physical phenomena that govern the motion of dislocations, focusing on those aspects that are connected to *dislocation glide* of *straight edge dislocations*. Climb, i.e. motion perpendicular to the plane, also occurs under certain circumstances but will not be treated, nor will cross slip (dislocation motion out of the original glide plane).

The driving force for glide is the Peach–Koehler force component given by (15). During glide, however, the dislocation may be subjected to various sources of resistance against motion. Denoting their collective force by  $\mathbf{f}_{\text{resist}}^{(I)}$  and ignoring inertia of dislocations, the motion of dislocation  $I$  is governed by the force balance

$$\mathbf{f}^{(I)} = \mathbf{f}_{\text{resist}}^{(I)}. \quad (16)$$

The two main contributions to the resistance of edge dislocations are:

- *Peierls–Nabarro stress*. As a dislocation moves, existing atomic bonds have to be broken and new ones formed. Because of the periodic nature of the lattice, the energy landscape that the dislocation moves across is periodic.

This acts as a *friction stress*, referred to as the Peierls–Nabarro stress, against the initiation of dislocation motion, corresponding to a resistance force of  $b\tau_f$  in the direction opposing the dislocation velocity  $v^{(I)}$ . The value of  $\tau_f$  depends sensitively on the crystal structure. At 0 K, the values for FCC and BCC crystals typically are  $10^{-6}\mu$  and  $10^{-3}\mu$ , respectively, while for intermetallics its value can be as large as  $0.1\mu$ .

- *Drag.* As a dislocation glides, it experiences drag originating from: (i) phonon drag; (ii) electron drag; (iii) impurity effects. Of these, phonon drag is dominating in many materials and gives a net, viscous force  $Bv^{(I)}$ . It is possible to make estimates of each of the contributions to phonon drag, but in practice  $B$  is measured experimentally or from molecular dynamics simulations. Values of  $B$  show quite some scatter; a typical value for aluminum is on the order of  $B = 10^{-4}$  Pa s. When drag is the only source of resistance, the balance (16) states

$$f^{(I)} = Bv^{(I)}$$

so that the velocity, for a given Peach-Koehler force, can be calculated from

$$v^{(I)} = f^{(I)} / B \quad (17)$$

A linear relationship between velocity and driving force has been confirmed experimentally. Data for various materials over various temperatures and stress levels suggest a relation of the type

$$v^{(I)} \propto (f^{(I)})^m e^{-E/k_B T}$$

but for relatively low stress levels, the exponent  $m$  is close to unity.

#### 4.1 Annihilation

Attraction of opposite-signed dislocations can lead to *annihilation*. This is easily seen for straight edge or screw dislocations of opposite sign coming close together: the defect is eliminated by coalescence of the dislocations once they are sufficiently close together. The critical annihilation distance is typically taken to be  $6b$ .

#### 4.2 Frank–Read sources

One possible mechanism for the generation of new dislocations is through the so-called Frank–Read mechanism illustrated in Fig. 5a. The source of this mechanism is a dislocation segment that is being pinned between two hard points. This segment bows out under the influence of a Peach-Koehler force, where the self-interaction helps to create a closed loop surrounding the initial pinned segment that finally closes onto itself. Ultimately, a smooth new dislocation loop has emerged

as well as a copy of the initial segment. This copy can operate as a source again, etc., so as to generate more dislocations.

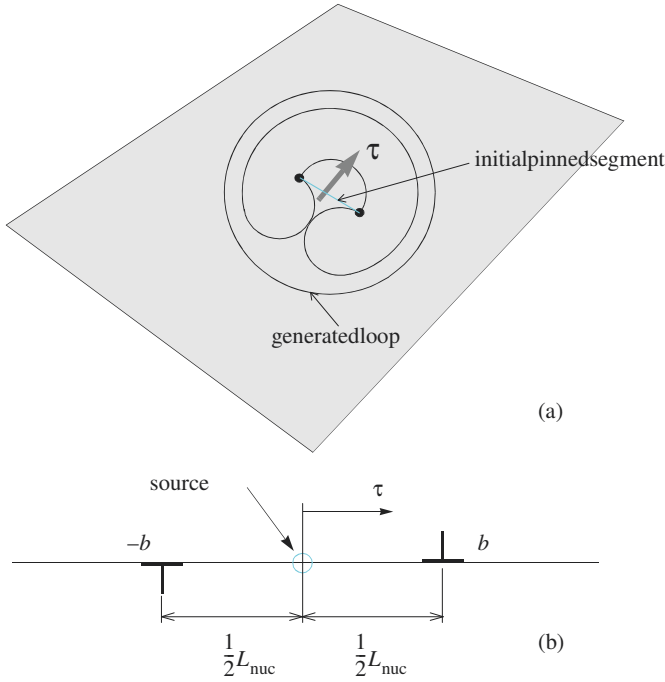


**Figure 5.** (a) Frank–Read mechanism of generating a new loop from an initial pinned segment. (b) Two-dimensional simplification (from [33]) as a mechanism for nucleation of edge dislocations.

Figure 5 shows a two-dimensional version of this mechanism, which one can imagine as a cross-section of a three-dimensional source and subsequent projection onto the plane of observation normal to the slip plane. The pinned segment now appears as a point, and the Frank–Read mechanism has been translated into two dimensions by [33] as follows. When the shear stress on the source is sufficiently high for a sufficiently long time, an edge dipole is generated. The strength of the source  $\tau_{nuc}$  is, in principle, determined by the three-dimensional dislocation configuration (initial segment length, Burgers vector, etc.); in the two-dimensional model it becomes a parameter. The same holds for the nucleation time  $t_{nuc}$ . The polarity of the dipole is determined by the direction of the shear stress. The width of the dipole,  $L_{nuc}$ , is the two-dimensional cross-section of the loop at the moment

that the initial pinned segment has been re-formed and the source is ready to operate again. The value of  $L_{nuc}$ , again, can be determined from three-dimensional simulations. However, a different and practical criterion has been proposed by [33] based on the observation that the dislocations in a dipole feel strong attractive forces that are inversely proportional to their distance. If this interactive force is larger than  $\tau_{nuc}b$ , the dislocations will move towards each other and annihilate so that effectively no dislocation has been generated. Hence, there is a minimum distance which is given by [33]

$$L_{nuc} = \frac{\mu b}{2\pi(1-\nu)\tau_{nuc}}.$$

## 5 Methodology for Crack Problems

The analysis of cracks and fracture within the framework of discrete dislocation plasticity employs the generic mode I problem sketched in Fig. 6. The calculations are carried out for small-scale yielding, with plasticity being confined to a window around the initial crack tip. Single-crystal studies (Secs. 6, 7) are performed by defining a set of two or three slip systems inside this window at an angle of  $\phi^{(\alpha)}$  with respect to the crack plane. Two slip systems are necessary to allow for any mode of plastic deformation, while three slip systems mimic the excess of available slip systems in a real three-dimensional FCC crystal. The process window is filled with a number of grains for the study of polycrystals in Sec. 8

Because of the assumed symmetry, there is a mirror dislocation for each dislocation in the region analyzed numerically. This mirror dislocation does not need to be accounted for explicitly when superimposing the fields of all dislocations, for example as in the sum in (15). Rather, its presence is accounted for through the symmetry boundary conditions. What does need to be accounted for in the dislocation analysis is that when a dislocation crosses the closed crack plane, it leaves the region analyzed; but, due to symmetry, a mirror dislocation enters into the system along the mirror slip plane.

The crack is initially sharp and a cohesive surface is laid out in front of it. At the scale of interest here, the cohesive surface is taken to mimic atomic debonding. Therefore, the constitutive response of the cohesive surface is taken from the universal binding law Rose *et al.* [31] and is specified by the following relation between the traction normal to the cohesive surface,  $T_n$ , and the separation  $\Delta_n$ :

$$T_n(\Delta_n) = \sigma_{\max} \frac{\Delta_n}{\delta_n} \exp\left(1 - \frac{\Delta_n}{\delta_n}\right), \quad (18)$$

As the cohesive surface separates, the magnitude of the traction increases, reaches a maximum and then approaches zero to represent the formation of a traction-free

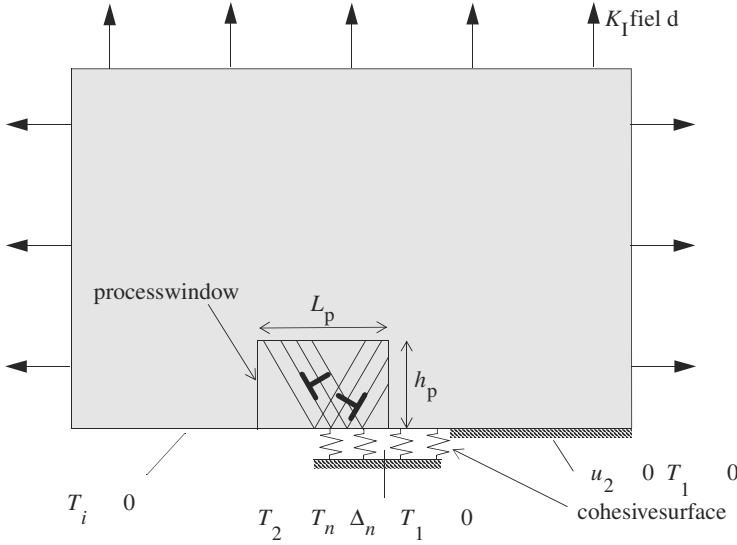


**Figure 6.** Small-scale yielding analysis under mode I conditions with discrete dislocations moving inside a process window. Because of symmetry, only half the problem needs to be analyzed. The cohesive surface ahead of the initial crack is used to describe crack growth.

crack, see Fig. 7. The strength  $\sigma_{\max}$  and the corresponding separation  $\delta_n$  characterize the fracture process, implying a work of separation  $\phi_n = \exp(1)\sigma_{\max}\delta_n$ . It is essential to note that the use of a cohesive surface eliminates the need of a fracture criterion: whether or not crack growth occurs is an outcome of the solution of the problem.

When studying a stationary crack, we take the value of  $\sigma_{\max}$  to be very large so as to avoid significant opening (yet, the purely elastic stress singularity of a mathematically sharp crack is always removed). Studies of crack growth by a cleavage mechanism are carried out by taking values  $\sigma_{\max} = 0.6 \text{ GPa}$  and  $\delta_n = 4b$ , giving a work of separation  $\phi_n = 1.63 \text{ J/m}^2$ . This value of the cohesive strength is about a factor of four smaller than the expected theoretical strength of aluminum and is used for numerical reasons because: (i) the length scale over which large gradients occur is inversely proportional to the cohesive strength, so that a finer mesh is required for higher values of the cohesive strength; and (ii) the number of dislocations increases with increasing cohesive strength, so that more dislocation interactions have to be computed and a larger process window is needed.

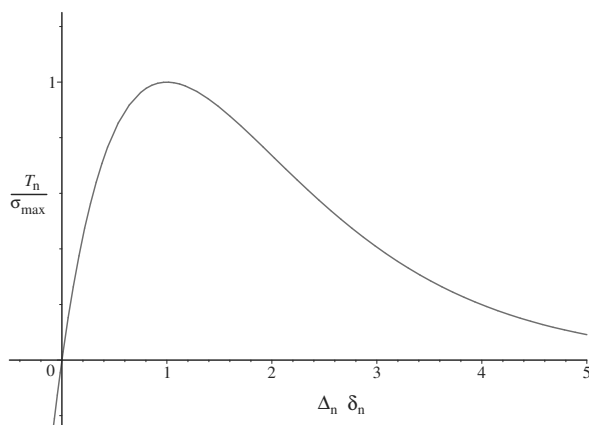


**Figure 7.** Traction–separation law corresponding to the universal binding law, according to (18).

The boundary conditions for the problem sketched in Fig. 6 are: (i) the crack faces remain traction free,  $T_i = 0$ ; (ii) the displacements on the remote boundary are specified according to the well-known elastic singular field; and (iii) for the symmetric mode I loading cases discussed here (18) is satisfied together with  $T_1 = 0$  on the crack plane ahead of the initial crack tip. The load level is thus characterized by the remote stress intensity factor  $K_I$ . In the absence of dislocation motion, the critical energy release rate is equal to  $\phi_n$ , from which we define the reference intensity factor  $K_0$  by

$$K_0 = \sqrt{\frac{E\phi_n}{1-\nu^2}}.$$

Because of the cohesive law (18), the problem sketched in Fig. 6 is nonlinear, and is solved in an incremental manner by phrasing the governing equations in rate form. Assuming that at time  $t$  the stress field and the current positions of all dislocations are known, the incremental (denoted by a superposed dot) ( $\dot{\phantom{x}}$ )-fields are governed by the virtual work statement

$$\begin{aligned} & \int_V \hat{\sigma}_{ij} \delta \epsilon_{ij} dV + \frac{1}{2} \int_{S_{\text{coh}}} k_n \left( \tilde{\Delta}_n^{(t+\Delta t)} + \hat{\Delta}_n^{(t)} \right) \hat{\Delta}_n \delta \Delta_n dS = \\ & - \frac{1}{\Delta t} \left[ \int_V \hat{\sigma}_{ij}^{(t)} \delta \epsilon_{ij} dV - \frac{1}{2} \int_{S_{\text{coh}}} T_n \left( \tilde{\Delta}_n^{(t+\Delta t)} + \hat{\Delta}_n^{(t)} \right) \delta \Delta_n dS \right] \end{aligned} \quad (19)$$

as shown by Cleveringa *et al.* [8]. Here, the instantaneous cohesive stiffness,  $k_n = -\partial T_n / \partial \Delta_n$ , and the instantaneous normal traction are evaluated at the fictitious opening  $\tilde{\Delta}_n^{(t+\Delta t)} + \hat{\Delta}_n^{(t)}$ . The factor 1/2 in (19) stems from the fact that, by virtue of symmetry, only half of the work in the cohesive surface contributes to the work in the region analyzed. The second integral in the left-hand side provides a contribution to the overall finite-element stiffness matrix that changes every time step; but computational costs can be reduced by factorizing the matrix except the part pertaining to the degrees of freedom connected to the cohesive elements.

## 6 Cracks in Single Crystals

A set of two or three slip systems is defined inside the window at an angle of  $\phi^{(\alpha)}$  with respect to the crack plane. Two orientations are considered, which are an approximation of the projections of three-dimensional orientations of FCC and BCC crystals respectively that lead to plane-strain plastic deformations [27]:

- FCC:  $\phi^{(1,2)} = \pm 60^\circ$  (or, more exactly  $\pm 54.6^\circ$ ), and  $\phi^{(3)} = 0$  when considering three slip systems;
- BCC:  $\phi^{(1,2)} = \pm 30^\circ$  (or, more exactly  $\pm 35.3^\circ$ ), and  $\phi^{(3)} = 90^\circ$  when considering three slip systems;

The calculations to be presented in subsequent sections do not aim at modeling a specific material, but properties representative of aluminum are used. The elastic properties are taken to be isotropic, with Young's modulus  $E = 70$  GPa and Poisson ratio  $\nu = 0.33$ . A representative value for the drag coefficient in (17) is  $B = 10^{-4}$  Pa s [19]. Unless otherwise noted, the strength of the dislocation sources is randomly chosen from a Gaussian distribution with mean strength  $\bar{\tau}_{\text{nuc}} = 50$  MPa and standard deviation  $0.2\bar{\tau}_{\text{nuc}}$ . The nucleation time for all sources is taken as  $t_{\text{nuc}} = 10$  ns. All obstacles are taken to have the same strength  $\tau_{\text{obs}} = 150$  MPa. Attention is focused on metal crystals with a relatively high density of initial defects, which are modeled by a random distribution of point sources and obstacles in the process window; there are no initial dislocations on the active slip systems in the simulations. Also, there is no special nucleation of dislocations from the crack tip.

### 6.1 Stationary Crack-Tip Fields

Figure 8 shows the stress distribution for an FCC crystal with three slip systems, and with such a high cohesive strength that the crack does not propagate. All three stress distributions exhibit large fluctuations, which are due to the singularities of the individual dislocations. In fact, the fluctuations shown are damped because of the way the contours are plotted on the finite element mesh that was used for the computation (80 by 80 elements in the process window).

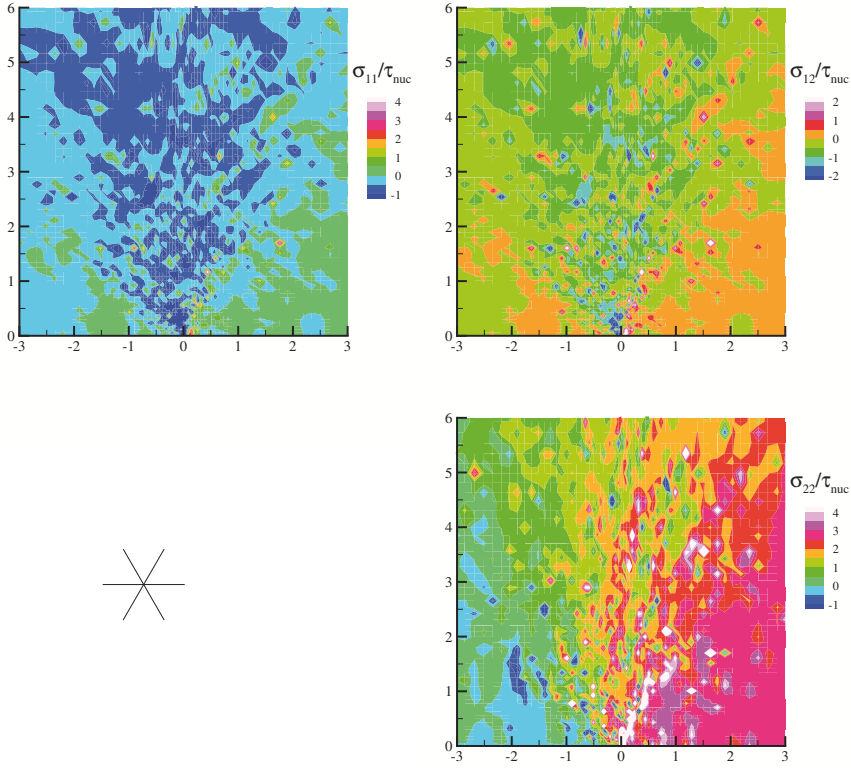


**Figure 8.** Stress distributions, normalized by the nucleation strength  $\tau_{nuc}$ , in an FCC crystal with three slip systems as indicated in the inset at  $K_I = 0.6\text{MPa}\sqrt{\text{m}}$ . From [34].

It is remarkable, however, that three sectors appear around the crack tip in which the stresses, on average, look different from one another. This stress distribution is reminiscent of the analytical near-tip stress field obtained by Rice [27] on the basis of a continuum plasticity theory for non-hardening crystals. When his analysis for the true FCC crystal geometry is modified to account for the set of slip systems used, four uniform stress sectors are obtained. The boundaries between these sectors are predicted to be  $60^\circ$ ,  $90^\circ$  and  $120^\circ$ , the first and last of which are consistent with the fields in Fig. 8. Van der Giessen *et al.* [34] carried out a quantitative comparison by actually averaging the stresses inside the four mentioned



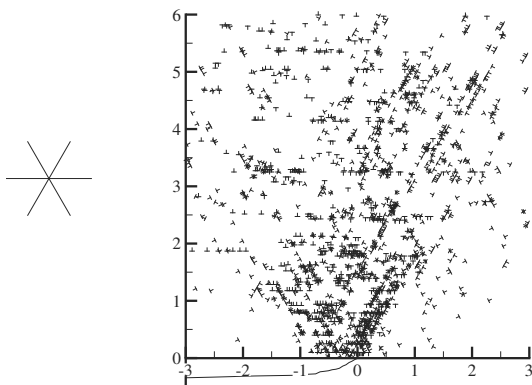


**Figure 9.** Dislocation distribution in the same crystal and at the same load level as in Fig. 8. From [34].

sectors, and it was found that these average stresses agreed quite well with Rice's continuum solution.

However, the discrete dislocation solution did not appear to agree with another element of Rice's [27] solution, namely that slip activity on the  $0^\circ$ -slip planes would concentrate in a kink band at  $90^\circ$ . The discrete dislocation results showed no evidence of this, as illustrated by the dislocation distribution shown in Fig. 9. The explanation for the absence of kink bands is that they would require an abundance of sources. Subsequently, Drugan [30] carried out an analysis similar to Rice's [27], but without requiring a kink band. He found several solution families, including a family of solutions which involve only a slip band at  $\theta = 60^\circ$ ; consistent with our discrete dislocation simulations. The solution that is closest to the discrete dislocation results is one where there are three sectors with boundaries at  $60^\circ$  and  $105^\circ$ . This solution is illustrated in Fig. 10. Even though the  $105^\circ$  sector boundary is not obvious from Fig. 8, averaging of the stress fields over these sectors showed very good agreement with this continuum prediction. Small differences in the exact average stress values are attributed to the fact that the continuum solution assumes no hardening, whereas some degree of hardening may occur in the discrete dislocation results.

## 6.2 Crack Propagation under Monotonic Loading

When averaging the discrete dislocation results over sectors to compare with the continuum plasticity predictions [34], the very near tip region with a radius of

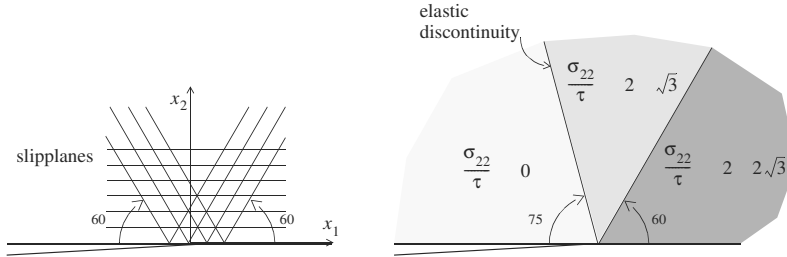


**Figure 10.** Opening stress states ( $\sigma_{22}$  normalized by the critical resolved shear stress  $\tau$ ) in the three sectors of Drugan's [30] continuum solution.

$0.5\mu\text{m}$  was excluded. The reason is that the stresses in this region are much higher than the sector averages, see Fig. 8. In fact, the results of Cleveringa *et al.* [8] suggest that the stresses in this region can become high enough for crack advance by cleavage (although, for numerical reasons, the cohesive strengths in the calculations are smaller than representative of actual metal cohesive strengths). This is illustrated in Fig. 11 for a case with two slip systems ( $\pm 60^\circ$ ) and with a cohesive surface characterized by the values  $\sigma_{\text{max}} = 0.6\text{GPa}$  and  $\delta_n = 4b$ . For these parameter values, the stationary crack tip blunts because of dislocation activity, Fig. 11a. The sector-average stresses at this instant are quite low, but the opening stress  $\sigma_{22}$  in a small region ahead of the crack reaches the cohesive strength. The crack then propagates until the crack tip arrives at a location where the near-tip opening stress is below the cohesive strength. Then, more dislocations are generated near the current tip, until the opening stress again reaches the strength, Fig. 11b, and the crack jumps forward again. This process of blunting and crack jumping continues as the load increases, giving rise to a distinct *R*-curve behavior.

It is worth emphasizing that in the calculations by Cleveringa *et al.* [8] there is no emission of dislocations from the crack tip. This is in contrast to simulations, e.g. by Hirsch and Roberts [13] and by Nitzsche and Hsia [14], where it is assumed that dislocations can be emitted only by the crack tip. The same assumption has been made in the analyses of mode III cracks by Zacharopoulos *et al.* [15]. This class of calculations aim at initially dislocation-free materials, such as silicon, where crack-tip emission is the key parameter in the transition from brittle fracture (no dislocations) to ductile fracture accompanied by dislocation motion, see also [12]. However, the model considered here is intended to mimic a metal in which there is an initial distribution of dislocations that act as Frank-Read sources or as forest dislocation obstacles.

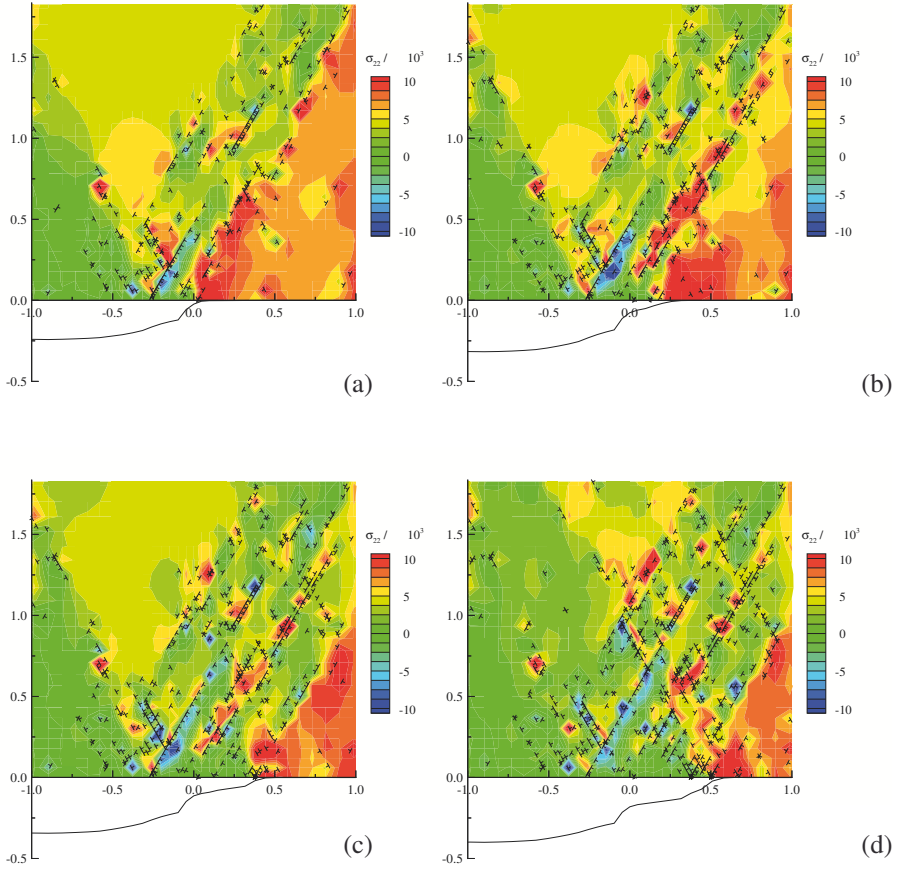


**Figure 11.** Distribution of dislocations and the opening stress  $\sigma_{22}$  in the immediate neighborhood ( $2\mu\text{m} \times 2\mu\text{m}$ ) of the crack tip for the FCC crystal with  $\rho_{\text{nuc}} = 49/\mu\text{m}^2$  and  $\rho_{\text{obs}} = 98/\mu\text{m}^2$  at four different stages of loading. The corresponding crack opening profiles (displacements magnified by a factor of 10) are plotted below the  $x_1$ -axis. From [8].

The main conclusion from the studies of Cleveringa *et al.* [8] is that dislocations play a dual role in fracture. On the one hand, dislocations are the vehicle for plastic deformation, and this reduces, on average, the stresses near the crack and provides a way to dissipate the energy flowing to the crack. On the other hand, dislocations can arrange themselves in structures, which lead to locally enhanced

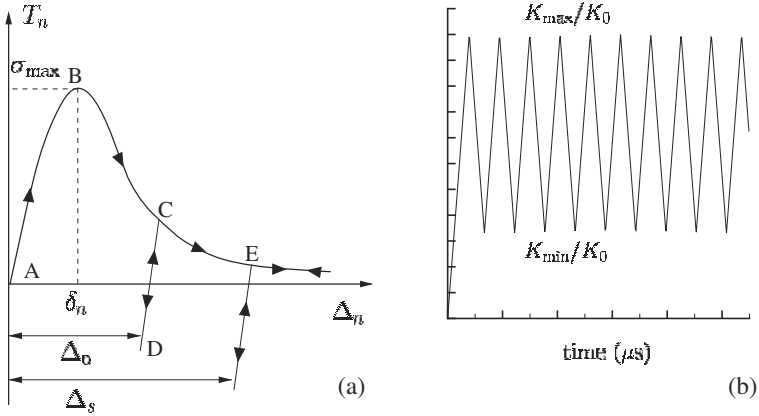


**Figure 12.** (a) Irreversible cohesive law used for fatigue calculations. (b) Schematic of the applied stress intensity factor as a function of time. From [10].

stress levels that can trigger crack growth. This stress enhancement is not modeled by conventional continuum plasticity.

## 7 Fatigue Crack Growth

Deshpande *et al.* [10] have extended the computations reported in the previous section to cyclic loading, specified by a remote stress intensity factor that zig-zags between  $K_{max}$  and  $K_{min}$ , Fig. 12b. The only change in the model is that the cohesive law is extended to be irreversible, as indicated in Fig. 12a, and which models the effect of complete oxidation of newly formed surface. This is a second source of irreversibility, next to the discrete dislocation plasticity, which is necessary for fatigue to occur.

Figure 13 summarizes the salient findings by Deshpande *et al.* [9, 10]:

1. The maximum stress intensity factor  $K_{max}$  needs to be high enough, i.e. above a critical value  $K_{max}^*$ , in order to provide a minimum of dissipation. For  $K_{max} \gg K_{max}^*$ , interactions within the now dense dislocation structure act to retard dislocation motion. Accordingly, a minimum cyclic stress intensity factor range  $\Delta K_I$  is needed to induce dislocation motion during unloading and reloading. Thus, in this regime,  $\Delta K_I$  below a critical *fatigue threshold* value  $\Delta K_{th}^*$  precludes crack growth.

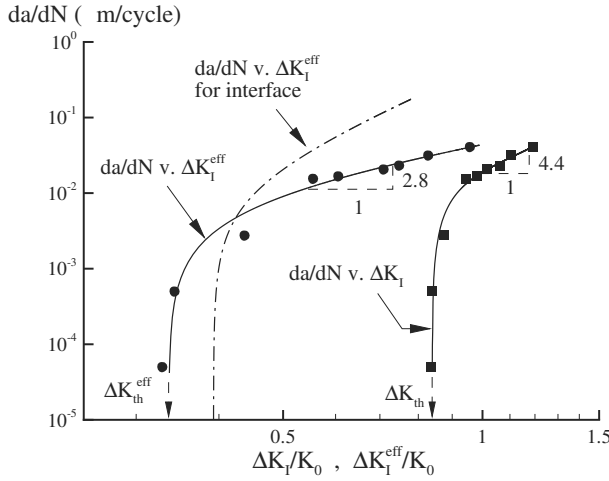


**Figure 13.** The cyclic crack growth rate  $da/dN$  versus  $\Delta K_I/K_0$  and  $\Delta K_I^{\text{eff}}/K_0$  for the mode I cyclic loading of a single crystal ( $R = K_{\min}/K_{\max} = 0.3$ ). The slopes of the curves marked correspond to the Paris law exponents for the curves fitted through the numerical results. From [10].

2. The curves of crack advance per cycle,  $da/dN$ , as a function of  $\Delta K_I$ , Fig. 13, show two distinct regimes of behavior: a steeply rising  $\log(da/dN)$  versus  $\log(\Delta K_I/K_0)$  curve in the threshold regime followed by a more gradual slope in the so-called *Paris regime*. The exponent  $m$  in the Paris relation

$$\frac{da}{dN} \propto (\Delta K_I)^m$$

for this case is  $\approx 4.4$ . When the same data is expressed in terms of the effective stress intensity range

$$\Delta K^{\text{eff}} = \begin{cases} K_{\max} - K_{\text{op}} & \text{for } K_{\min} < K_{\text{op}} \\ \Delta K_I & \text{for } K_{\min} \geq K_{\text{op}}, \end{cases}$$

where  $K_{\text{op}}$  is the stress intensity at which the crack faces first separate [9], the Paris exponent is only around 2.8.

A fit  $da/dN$  versus  $\Delta K_I^{\text{eff}}/K_0$  curve for an interface crack is also plotted in Fig. 13. The effect of the mode mixity at the interface is to increase the fatigue threshold of the interface crack but to reduce its resistance to cyclic crack growth at higher values of applied  $\Delta K_I$ . This behavior is expected to be dependent on

the degree of mode mixity and hence affected by the cohesive properties and the applied loading.

Based on the experimental work of Laird and Smith [20] and Neumann [21], fatigue crack growth in ductile metals is often presumed to occur by an alternating slip mechanism which is a deformation-controlled phenomenon that does not require high stresses. On the basis of this, Pippan and co-workers [23, 24] and Wilkinson *et al.* [25] developed discrete dislocation models to represent this deformation-controlled fatigue crack growth mechanism. These models incorporate the crack growth mechanism as an ingredient of the model rather than have it emerge as a prediction of the analysis. By contrast, in the framework presented here [9, 10] fracture is both a deformation and stress-governed phenomenon and takes place by a mechanism that is possible under both monotonic and cyclic loading conditions. Striations are also predicted by the model, as shown in Fig. 14.

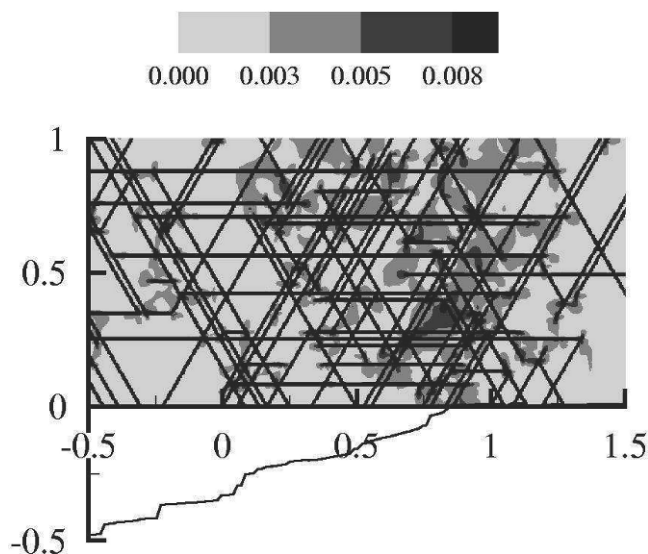


**Figure 14.** Contours of total slip showing the localized deformation pattern in the crack tip vicinity. All distances are in  $\mu\text{m}$ . The crack opening profile (displacements magnified by a factor of 20) is plotted below the  $x_1$ -axis. From [10].

## 8 Cracks in Polycrystals

Finally, we look at the crack tips fields in polycrystals, cf. Fig. 1c. For this purpose, the problem in Fig. 15b is analyzed, where the process window now contains a number of square grains. A mixture of FCC and BCC grains are considered, arranged in a checker-board pattern, Fig. 16; results will be presented here mainly for the case where the crack tip is in an FCC grain, Fig. 16a. All grains have the same density of sources,  $\rho_{\text{nuc}} = 20 \mu\text{m}^{-2}$  with average strength  $\bar{\tau}_{\text{nuc}} = 46 \text{ MPa}$  and standard deviation  $9.2 \text{ MPa}$ ;  $\rho_{\text{obs}} = 40 \mu\text{m}^{-2}$  in all grains. The grain size  $d$  is taken to vary between  $0.2 \mu\text{m}$  and  $d = 5.0 \mu\text{m}$ .

In a continuum view, and assuming overall isotropic behaviour, the HRR solution for the opening stress is of the type

$$\sigma_{22} \propto \left( \frac{1}{r} \right)^{\frac{1}{s+1}} \quad (20)$$

where  $s$  is the strain hardening exponent in a shear stress  $\tau$  versus shear strain  $\gamma$  relation of the form  $\gamma \propto \tau^s$ . The overall stress-strain behaviour of the polycrystals is extracted from pure shear computations on the grains inside the process window, as illustrated in Fig. 15a. The results in Fig. 17 show that the response is strongly dependent on the grain size. The shear stress between  $\gamma = 0.15\%$  and  $0.25\%$ ,  $\bar{\tau}$ , as a measure of yield stress, can be fit to the Hall-Petch type relation

$$\bar{\tau} - \tau_0 = \beta \left( \frac{d}{d_0} \right)^{-q}, \quad (21)$$

with an exponent  $q = 0.415$  when using  $\tau_0 = 20 \text{ MPa}$ , the flow strength of a single crystal, and taking the reference grain size  $d_0 = 1 \mu\text{m}$ . The Hall-Petch effect in these computations arises from the fact that grain boundaries act to stop the motion of dislocations.

The differences in deformation fields in polycrystalline aggregates with different grain size are represented in Fig. 18 in terms of the total slip

$$\Gamma = \sum_{\alpha=1}^3 |\gamma^{(\alpha)}|, \quad \gamma^{(\alpha)} = s_i^{(\alpha)} \varepsilon_{ij} m_j^{(\alpha)}.$$

While the total density of sources and obstacles is independent of grain size and the same as for the single crystal, Fig. 18a, the slip distribution becomes smoother as the grain size decreases (note that the process window has the same dimensions). To show two extreme cases, Fig. 19 gives the stress distributions in a single crystal and in a polycrystal with small grains,  $d = 0.6 \mu\text{m}$ . In contrast to the single crystal response (as discussed previously), the stress distribution inside the polycrystal is

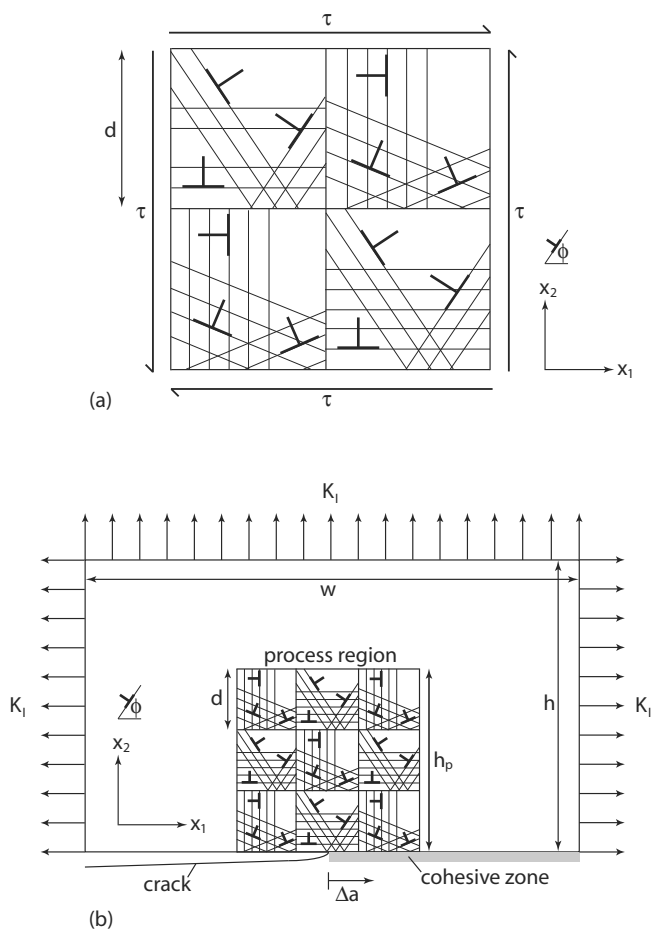


**Figure 15.** Sketch of (a) the pure shear problem with doubly-periodic boundary conditions and (b) the small scale yielding crack problem with imposed mode I loading. From [3].

seen to more closely resemble the isotropic HRR predictions. Thus, both the stress and strain fields around the crack tips in our polycrystal analyses indicate that the grain boundaries successfully block the formation of slip bands and tend to diffuse plastic deformation which results in more isotropic distributions of stress and strain.



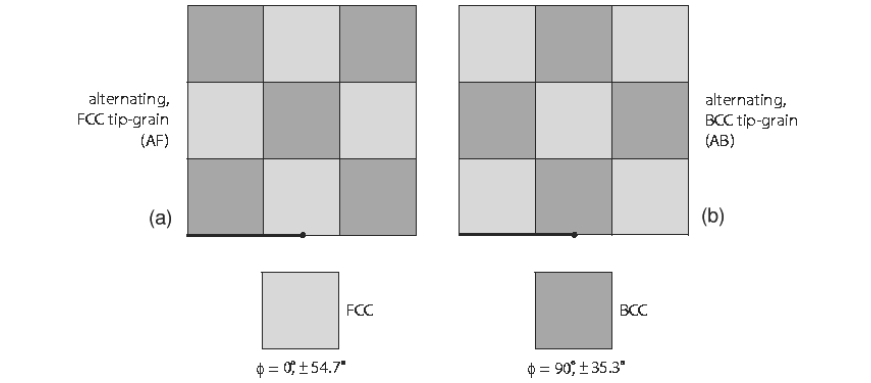


**Figure 16.** Two polycrystalline grain arrangements used in the mode I crack simulations. The arrangements are illustrated for a  $3 \times 3$  array of grains with the crack plane indicated by the dark line. From [3].

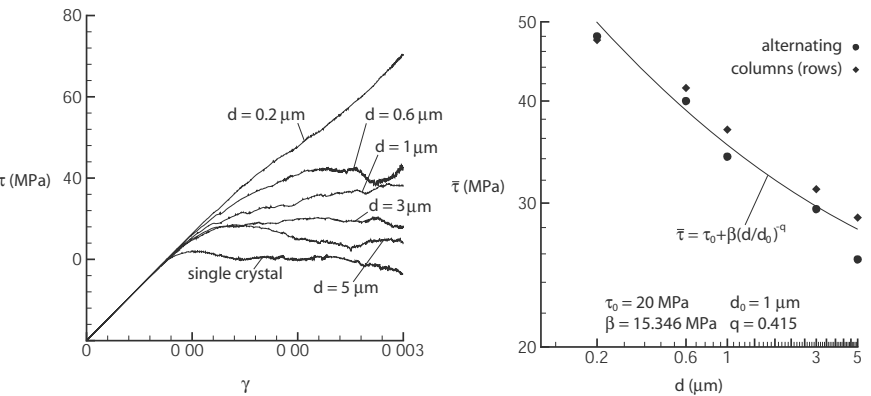


**Figure 17.** (a) Applied shear stress  $\tau$  versus shear strain  $\gamma$  response of the polycrystalline and single crystal materials analyzed in this study. (b) Average shear stress  $\bar{\tau}$  between  $\gamma = 0.15\%$  and  $0.25\%$  for both grain arrangements as a function of grain size  $d$ . The Hall–Petch type relation eq. (21) is fit to the data. From [3].

The distribution of the opening stress ahead of the crack tip, Fig. 20, reveals three distinct regimes. Sufficiently far from the tip,  $\sigma_{22} \propto 1/\sqrt{r}$  according to the

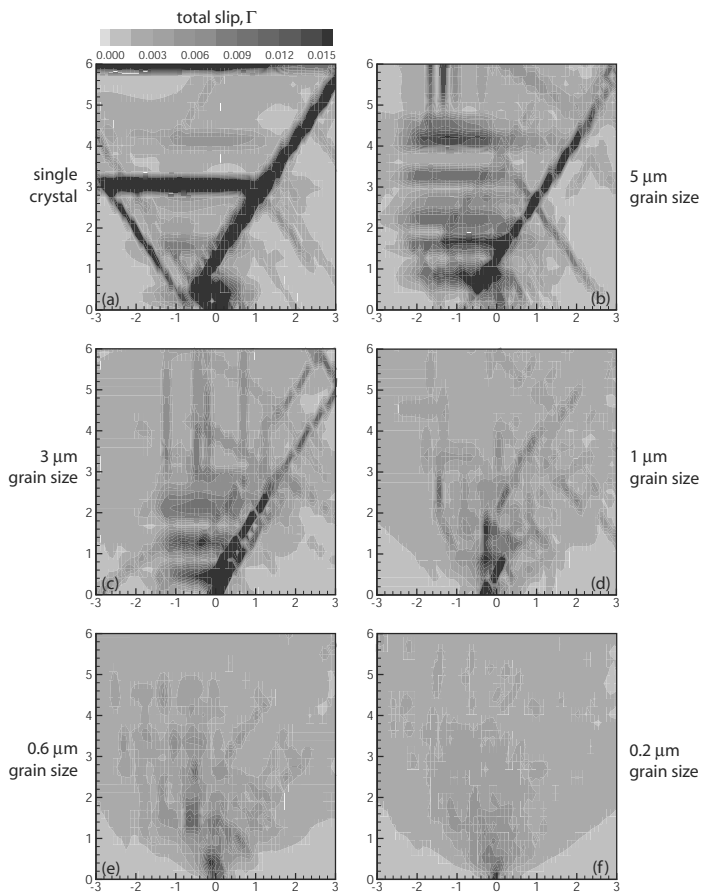


**Figure 18.** Distributions of total slip  $\Gamma$  around the stationary crack tip of polycrystals at an applied  $K_I/K_0 = 1.75$ : (a) pertains to the FCC single crystal and (b) through (f) are for the  $d = 5\mu\text{m}$  to  $d = 0.2\mu\text{m}$  polycrystals, in descending order. (All distances are in  $\mu\text{m}$ .) From [3].

elastic  $K$ -field, while very close to the tip the discreteness of the dislocations governs the field. In between there is a regime which has been fitted to a power-law consistent with the HRR field (20).

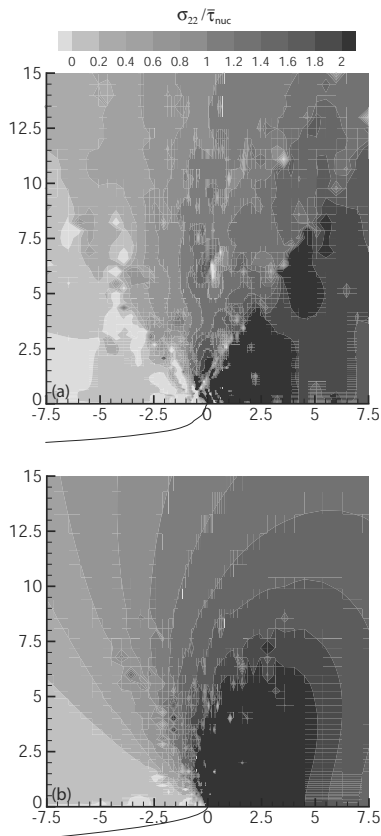


**Figure 19.** Distributions of normalized stress,  $\sigma_{22}/\bar{\tau}_{nuc}$ , around the stationary crack tip at  $K_I/K_0 = 1.75$ : (a) the FCC single crystal (b) the polycrystal with  $d = 0.6 \mu m$ . The crack-tip profile with displacement magnified by a factor of 50 is included in both cases. (All distances are in  $\mu m$ .) From [3].

## Bibliography

- [1] R.J. Asaro, *Adv. Appl. Mech.* **23**, 1–115 (1983).
- [2] M.F. Ashby, *Phil. Mag.*, **21**, 399 (1970).
- [3] D.S. Balint, V.S. Deshpande, A. Needleman and E. Van der Giessen, *Philos. Mag.* **85** (2005).

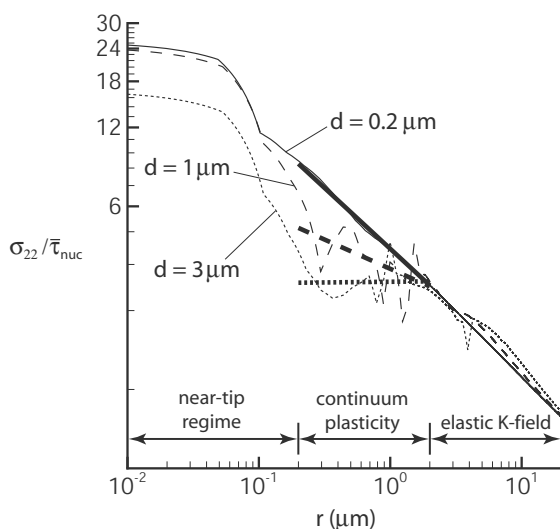


**Figure 20.** Normalized crack opening stress,  $\sigma_{22}/\bar{\tau}_{nuc}$ , on the crack plane ahead of the stationary crack tip at an applied  $K_I/K_0 = 1.75$  for the polycrystal. Thick lines are fits to an HRR field for the continuum plasticity regime. From [3].

- [4] W.D. Callister, *Materials Science and Engineering: An Introduction*. Fifth Edition. John Wiley & Sons, New York, 2000.
- [5] E. Van der Giessen, *Mechanics of Microstructured Materials*, ed. by H.J. Bhm, CISM Courses and Lectures No. 464, 259–282 (2004).
- [6] H.H.M. Cleveringa, E. Van der Giessen and A. Needleman, *Acta Mat.* **45**, 3163–3179 (1997).
- [7] H.H.M. Cleveringa, E. Van der Giessen and A. Needleman, *Int. J. Plast.* **15**, 837–868 (1999).
- [8] H.H.M. Cleveringa, E. Van der Giessen and A. Needleman, *J. Mech. Phys. Solids* **48**, 1133–1157 (2000).
- [9] V.S. Deshpande, A. Needleman and E. Van der Giessen, *Acta Mat.* **49**, 3189–3203 (2001).
- [10] V.S. Deshpande, A. Needleman and E. Van der Giessen, *Acta Mat.* **50**, 831–846 (2002).
- [11] V.S. Deshpande, A. Needleman and E. Van der Giessen, *Acta Mat.* **51**, 1–15 (2003).
- [12] P. Gumbsch, J. Riedle, A. Hartmaier, H.F. Fischmeister, *Science* **282**, 1293–1295 (1998).

- [13] P.B. Hirsch, S.G. Roberts, *Scr. Metall.* **23**, 925–930 (1989).
- [14] V.R. Nitzsche, K.J. Hsia, *Mat. Sci. Engng.* **A176**, 155–164 (1994).
- [15] N. Zacharopoulos, D.J. Srolovitz, R. LeSar, *Acta Mat.* **45**, 3745–3763 (1997).
- [16] J.P. Hirth and J. Lothe, *Theory of Dislocations*. McGraw–Hill, USA, 1968.
- [17] D. Hull and D.J. Bacon, *Introduction to Dislocations*. Fourth Edition, Butterworth–Heinemann, UK, 2001.
- [18] J.W. Hutchinson, *J. Mech. Phys. Solids* **16**, 13–31 (1968).
- [19] L.P. Kubin, G. Canova, M. Condat, B. Devincere, V. Pontikis, Y. Bréchet, *Solid State Phenomena* **23 & 24**, 455–472 (1992).
- [20] C. Laird and G.C. Smith, *Phil. Mag.* **7** 847–857 (1962).
- [21] P. Neumann, *Acta Metall.* **17**, 1219–1225 (1969).
- [22] J.F. Nye, *Acta. Metall.* **1**, 153 (1953).
- [23] R. Pippan, *Acta Metall. Mat.* **39**, 255–262 (1991).
- [24] F.O. Riemelmoser, P. Gumbsch, R. Pippan, *Mat. Trans. JIM* **42**, 2–13 (2001).
- [25] A.J. Wilkinson, S.G. Roberts, P.B. Hirsch, *Acta Mat.* **46**, 379–390 (1998).
- [26] J.R. Rice and G. Rosengren, *J. Mech. Phys. Solids* **16**, 1–12 (1968).
- [27] J.R. Rice, *Mech. Mater.* **6**, 317–335 (1987).
- [28] J.R. Rice and J.-S. Wang, *Mat. Sci. Engin.* **A107**, 23–40 (1989).
- [29] M. Saeedvafa, J.R. Rice, *J. Mech. Phys. Solids* **37**, 673–691 (1989).
- [30] W. Drugan, *J. Mech. Phys. Solids* **49**, 2155–2176 (2001).
- [31] J.H. Rose, J. Ferrante, J.R. Smith, *Phys. Rev. Lett.* **47**, 675–678 (1981).
- [32] J.Y. Shu, N.A. Fleck, E. Van der Giessen and A. Needleman, *J. Mech. Phys. Solids* **49**, 1361–1395 (2001).
- [33] E. Van der Giessen and A. Needleman, *Model. Simul. Mater. Sci. Eng.* **3**, 689–735 (1995).
- [34] E. Van der Giessen, V.S. Deshpande, H.H.M. Cleveringa and A. Needleman, *J. Mech. Phys. Solids* **49**, 2133–2153 (2001).
- [35] E. Van der Giessen and A. Needleman, *Scripta Mat.* **48**, 127–132 (2003).